# Unraveling Climatic Wind and Wave Trends in the Red Sea Using Wave Spectra Partitioning

SABIQUE LANGODAN

*Red Sea Research Center, King Abdullah University of Science and Technology, Thuwal, Saudi Arabia*

LUIGI CAVALERI AND ANGELA POMARO

*Institute of Marine Sciences, CNR-ISMAR, Venice, Italy*

JESUS PORTILLA

*Department of Mechanical Engineering, Escuela Politécnica Nacional, Quito, Ecuador*

YASSER ABUALNAJA

*Red Sea Research Center, King Abdullah University of Science and Technology, Thuwal, Saudi Arabia*

IBRAHIM HOTEIT

*Physical Sciences and Engineering Division, King Abdullah University of Science and Technology, Thuwal, Saudi Arabia*

(Manuscript received 8 May 2017, in final form 12 December 2017)

ABSTRACT

The wind and wave climatology of the Red Sea is derived from a validated 30-yr high-resolution model simulation. After describing the relevant features of the basin, the main wind and wave systems are identified by using an innovative spectral partition technique to explain their genesis and characteristics. In the northern part of the sea, wind and waves of the same intensity are present throughout the year, while the central and southern zones are characterized by a marked seasonality. The partition technique allows the association of a general decrease in the energy of the different wave systems with a specific weather pattern. The most intense decrease is found in the northern storms, which are associated with meteorological pulses from the Mediterranean Sea.

## 1. Introduction

When the Arabian Peninsula split from the Horn of Africa in the Eocene and Oligocene eras, it created the Great Rift Valley in the northeast part of Africa and led to the progressive opening of the Red Sea. The shape of the area reflects its genesis. It is a very long, narrow basin (see Fig. 1), more than 2200 km long and with an average width of 180 km, 355 km at its widest span. High mountain ranges border both sides of the Red Sea, and the highest point is more than 4000 m above sea level in the Ethiopian high plains. These mountain ranges are instrumental in establishing the local weather patterns; most of the time, winds blow along the longitudinal axis of the basin. At its southern end, the Bab el Mandeb connects the Red Sea to the Gulf of Aden and the Arabian Sea (see the inner panel in Fig. 1). During the winter months, the high mountains south of the strait force the northeast monsoon winds to turn right and funnel through the strait, blowing northward over the Red Sea (Langodan et al. 2014).

Few studies have investigated the wave conditions in the Red Sea. Metwally and Abul-Azm (2007) generated a wave atlas using a low-resolution (0.25°) wave model forced by coarse-resolution (1.9°) wind speeds from the NCEP reanalysis. The spatial and temporal variability of Red Sea waves was also investigated by Fery et al. (2012) using a low-resolution (0.25°) simulating waves nearshore (SWAN) model forced with the global meteorological model (GME) of the German meteorological service

*Corresponding author*: Ibrahim Hoteit, ibrahim.hoteit@kaust.edu

DOI: 10.1175/JCLI-D-17-0295.1

(DWD). Ralston et al. (2013) presented a description of wave conditions in the Red Sea from a two-year simulation of a coupled SWAN–advanced circulation model (ADCIRC) system, configured at 5-km resolution. Langodan et al. (2014) explored how well the general and unusual wind and wave patterns of the Red Sea could be reproduced using standard meteorological products and local wind and wave models. Recently, Langodan et al. (2016) and Aboobacker et al. (2016) presented an assessment of wave energy potentials in the Red Sea from long-term wave model simulations.

In this work, we use 30 yr of wind and wave conditions to analyze the climatic features of the Red Sea, focusing on the dominant wind and wave regimes. The extent of the available data further allows us to identify possible trends in the wind and the wave integral parameters. Many studies of the wind-wave climate have been conducted on both global (e.g., Wang and Swail 2001; Caires et al. 2006; Vinoth and Young 2011; Semedo et al. 2011; Gulev et al. 2003) and regional [e.g., Kushnir et al. (1997) for the North Atlantic Ocean, Tuomi et al. (2011) for the Baltic Sea, Charles et al. (2012) for Atlantic coasts, Appendini et al. (2014) for the Gulf of Mexico, Semedo et al. (2015) for the Nordic seas, and Liu et al. (2016) for the Arctic Ocean] scales. Most of the studies dealing with wave climate variability are broadly focused on statistical or integrated wave parameters, such as significant wave height, mean wave period, and mean wave direction. Here we present an innovative approach based on Portilla et al. (2015), in which we analyze the statistics of wave spectra in the Red Sea using a partition technique that further allows us to identify the origins of the observed trends and the associated tendencies in the larger-scale driving conditions.

The structure of the paper is as follows. We provide a brief description of the dominant wind and wave systems in the Red Sea in section 2. In section 3, we describe the methodology followed for the hindcast. Section 4 presents the first part of the results, including the general climatology of the area and highlighting special conditions connected to the orography of the basin. We investigate the possible trends of waves in time by focusing on the temporal variability of the wind and wave data in section 5. This is further investigated in section 6, where we identify the origin of the various trends using the spectral partition technique. We summarize our findings in section 7, where we also point out how the net results for a particular area, the Red Sea being the example here, may help to shed light on climate trends on a much larger scale.

## 2. Wind and waves in the Red Sea

A brief description of the wind and wave characteristics of the Red Sea can be found in Fig. 1. Indicated by arrows in the figure are four wind systems (systems E1, E2, E3, and E4 in Table 1) that dominate the situation.

System E1 is driven by pulses from the Mediterranean Sea—either by the typical storms of the non-summer months or by the Etesian winds over the Aegean Sea during the hot season. The pulses move across the Nile delta (see the side panel in Fig. 1) and the Gulf of Suez and then propagate southward as an energetic, relatively cold front. Based on yearly averages, these are the most energetic waves in the basin, propagating until the southern end of the Red Sea, often as swell and frequently as wind sea when the weather front propagates to the south (Langodan et al. 2014).

System E2 is present from October to April and is considered the most regular wind regime in the southern Red Sea. The waves generated by E2 propagate northward, strongly attenuating as they approach the northern end of the Red Sea. If both the E1 and the E2 systems are present, a very peculiar, almost unique situation may appear in the Red Sea. When a pulse from the Mediterranean enters the basin and an extended E2 system is present, these two opposing wind systems converge around the center of the Red Sea. The warmer E2 air ascends above the southward-moving, colder air from the north, leading to a peculiar local situation of cloudiness and drizzle in the middle of a vast sunny area. Langodan et al. (2014) provided a full description of this situation. This is complex for waves, where we have the unique case of two opposing wind-wave systems, both in their active generation zones. Langodan et al. (2015) showed that the physics used in the present wave models need to be updated to better simulate these opposing wave conditions. This updated term is not used in the current 30-yr hindcast because it has not been sufficiently tested under all possible conditions. While physically relevant, the implications of the ''encounter'' condition, which is limited in space and time, are marginal for the overall statistics.

The third system, E3, is associated with the Tokar Gap wind that blows in the summer, from July to September (Jiang et al. 2009). The variability of E3 is controlled by the summer wind regimes, as it occurs at a crossroad of influences from the seasonal Indian Ocean monsoon cycle to the south and the seasonal patterns of the Sahara Desert and the eastern Mediterranean Sea to the north (Pedgley 1974). The system E3 is also influenced by the local Red Sea land–sea breeze cycle, especially the thermally driven wind that originates from the night cooling on the African high plains, which propagates down through the Tokar Gap with a katabatic effect toward and across the Red Sea (see Fig. 1 for its position). This wind generates the highest waves in the Red

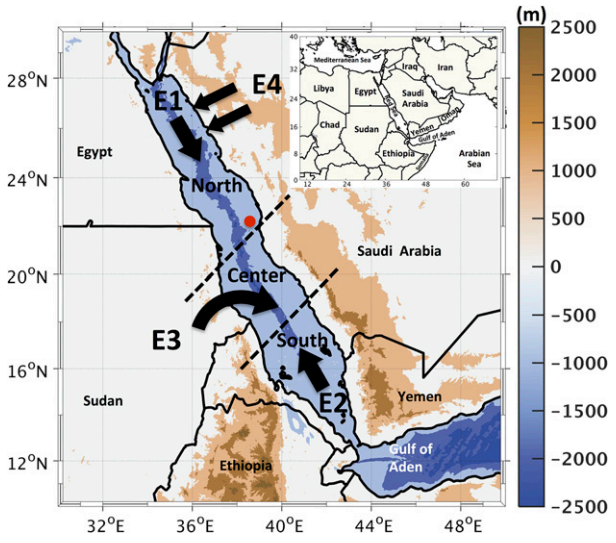


FIG. 1. The Red Sea is more than 2200 km long and 350 km across at its widest point. The topography is shown by the color shades. The dashed lines split the basin into three zones: N, C, and S. The arrows indicate the main winds blowing in the basin. The side panel frames the position of the basin within a larger geographical area. The red dot shows the position of the buoy.

Sea (up to and more than 5 m), especially when they interact with the E1 system.

The least globally important but still locally relevant system is the E4 system, which describes the jets that blow down through narrow valleys in the northern part of the Arabian Peninsula, leading to locally high waves (Jiang et al. 2009). Other wind and wave patterns appear occasionally but are not permanent or consistent enough to be considered relevant in the local climatology.

## 3. 30-yr hindcast

The Advanced Research version of the Weather Research Forecasting (WRF-ARW; Skamarock et al. 2008) mesoscale model was used to generate the high-resolution wind fields over the Red Sea and its adjoining region. The model was implemented with two two-way nested grids; the outer domain covers 5°–39°N, 15°–63°E with 30-km resolution, and the inner domain focuses on 7°–32°N, 30°–52°E with 10-km resolution.

The ERA-Interim reanalysis fields (Dee et al. 2011) were used as the initial and boundary conditions. The model was initialized on a daily basis at 1200 UTC and integrated for 36 h using boundary conditions that were updated every 6 h. Assimilation of the available observations in the region, collected from the National Centers for Environmental Prediction (NCEP) Atmospheric Data Project (ADP; 1997 to present), was conducted in six-hour cycles using a three-dimensional variational (3DVAR) approach. For the WRF-ARW assimilation, we combined all the observations available for the previous years from different sources. The hourly outputs from +12 until+36 h of the simulation were used as results of the hindcast. These hourly wind fields were used to force a regular grid with the 0.05°-resolution WAVEWATCH III (WW3) wave model (Tolman 2014), implemented with 29 frequencies ($f_1$ = 0.05 Hz) with 1.1 geometric progressions and 36 directions uniformly distributed starting at 5°. The most recent version of WW3 as available since 2014 has been used, with the latest generation and dissipation physics of Janssen (1991) and Ardhuin et al. (2010). As in all the operational models and long-term hindcasts, the discrete interaction approximation (DIA) formulation of Hasselmann et al. (1985) has been used for nonlinear interactions.

Concerning the results, Langodan et al. (2016) reported a low bias for both wind and waves when compared to the available measured data (from buoys, scatterometers, and altimeters). Best-fit slopes, bias, rms error, and scatter index from buoy were 0.99, −0.07, 1.63, and 0.31 for wind speed (m s$^{-1}$) and 1.01, 0.03, 0.24, and 0.26 for significant wave height (m) (additional details are provided in the appendix). These values are amply suitable for a climatological analysis. More details about the validation of the model results are provided in the appendix.

## 4. Wind and wave climatology of the Red Sea

The left panel of Fig. 2 shows the spatial distribution of the mean wind speed $U_{10}$ and significant wave height

TABLE 1. Dominant wind and wave systems in the Red Sea.

| System | Characteristics |
|---|---|
| E1 | This system blows from northwest to southeast year-round, often extending to the southern end of the basin. |
| E2 | Associated with the northeast monsoon, it blows to the northwest from the southern end of the basin, typically extending well into the Red Sea during the winter season. |
| E3 | The Tokar Gap wind blows through the valley located halfway down the African coast; it is highly associated with the summer monsoon and differential heating, is present during the summer months, and generates the highest waves in the basin. |
| E4 | Jets exiting from narrow valleys in the northern part of the Arabian Peninsula cause waves that are not very high but that may be superimposed on those of system E1. |

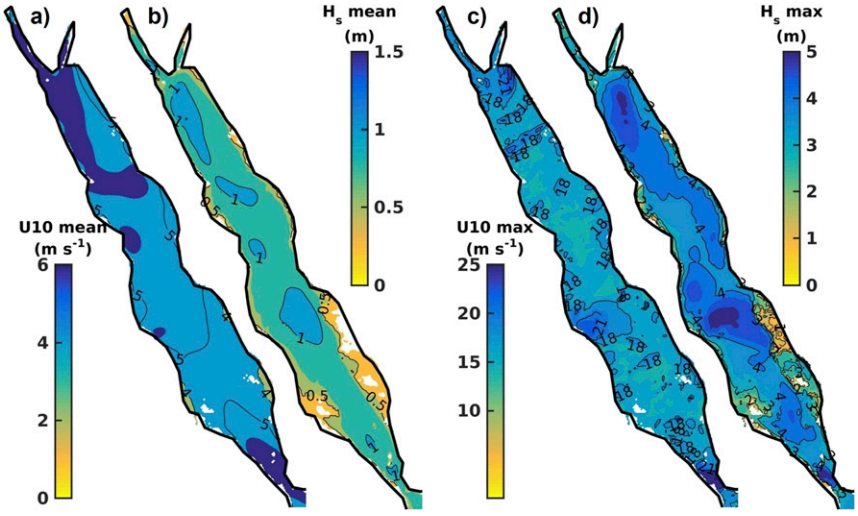


FIG. 2. Wind and wave climatology of the Red Sea. (a),(b) Mean wind speed and significant wave height distributions, respectively. (c),(d) As in (a),(b), but for the maximum values.

$H_s$. The right panel provides the corresponding maximum values from the period covered in our study. There are three clear zones of intense action: (i) in the northern part of the Red Sea, due to the E1 system, (ii) in the center, due to the Tokar Gap (E3), and (iii) at the southern end, due to the northeast monsoon winds of E2. The differences between the mean and maximum values are more evident in the central and southern zones, as a consequence of the more marked seasonality of the winds in these two areas. As expected, these differences are less pronounced when analyzed on a seasonal basis. This is particularly relevant for the E2 system, which is connected to the winter northeast monsoon, though the differences are still large for the Tokar Gap winds (E3), owing to their diurnal variations.

In this respect, more complete information is provided in Fig. 3, where we report the statistical distribution of $U_{10}$ and $H_s$ in each of the three zones: north (N), center (C), and south (S) (separated by the two dashed lines in Fig. 1). These zones correspond to the dominance of the E1, E3, and E2 systems, respectively. With some limited variability, E1 winds are present over N throughout the year and are often strong compared to the other zones. E2 and E3, in S and C, respectively, blow seasonally and are mostly in a lower range of values. However, the most frequent high values occur in C, following the Tokar Gap winds. The distributions of the wave heights over the 30-yr period (Fig. 3; mean $H_s$ in the left panel, maximum $H_s$ in the right panel) show similar information, although less pronounced, due to the integral properties of the waves with respect to the generating wind fields.

An interesting characteristic of the local climate is revealed by the annual distribution of the wind speeds and significant wave heights in the three zones. The daily averages of these two variables (on the left and right panels, respectively) over each zone, and their corresponding running averages, the 95th and 5th percentiles, are plotted in Fig. 4. Wind and waves are permanently present in the northern Red Sea, and the higher values (95 percentile) in particular are noticeable throughout the year. With some undulations during the summer (corresponding to the Etesian winds), wind and waves are always active in this area, with the daily $H_s$ mean close to 1 m (with the exception of slightly lower values between July and August). This suggests changes in the climate of the Mediterranean basin and the African region.

The Mediterranean Sea acts as a border between the European climate to the north and the tropical climate of the African continent, restricting the interactions between these two drastically different regimes. The Red Sea and its two northern gulfs (Suez and Aqaba) provide the only pathways for meteorological pulses to flow southward, connecting the northern and southern regimes throughout the year. In contrast to N, the distribution is seasonal in C and S. The presence of the Tokar Gap winds is evident in Figs. 4b and 4e. The lower wave heights observed in October suggest that the northerly waves are not developed enough to reach the C or, a fortiori, S zones. This could be attributed to the beginning of the monsoon-associated southern winds (Figs. 4c,f) in this period. In S, the seasonality of the southern winds is more strongly manifested by the wave plot (Fig. 4f), suggesting that some of the winds over the region (Fig. 4c) are not associated with the monsoon.

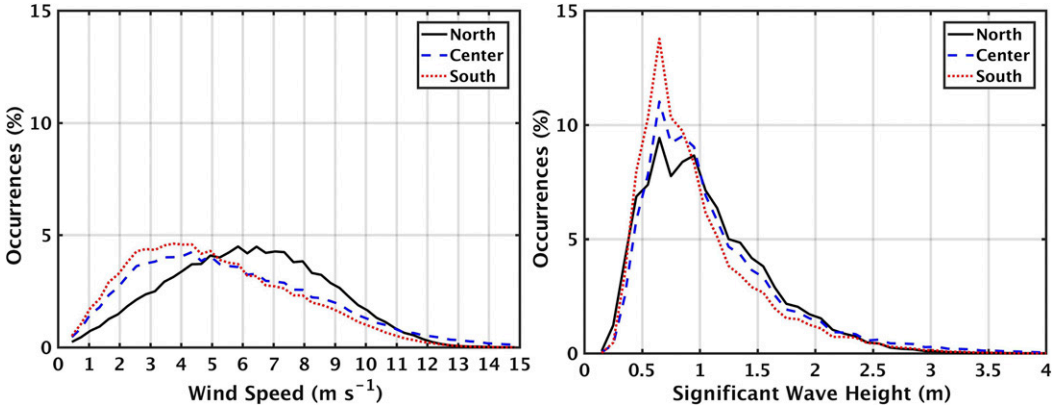


FIG. 3. Statistical distribution of (left) wind speed $U_{10}$ and (right) significant wave height $H_s$ in the three areas: N (black solid), C (black dashed), S (red dotted) indicated in Fig. 1.

## 5. Time variability

After assessing the general characteristics and seasonality of the wind and waves in the Red Sea, and taking advantage of the long (30 yr) time series for all of the parameters of interest, we explore the possible trends in time.

Similar to Fig. 3, we present in Fig. 5 the statistical distribution of $U_{10}$ and $H_s$ in the basin for the first (1985–94), middle (1995–2004), and last decade (2005–14) of the studied period. A shift in time toward lower values is evident, both for wind and waves. For instance, the peak of the $U_{10}$ distribution in $N$ lowered from 6.5 to 5.8 m s$^{-1}$. The decrease is more noticeable in the wave height distribution, where the number of large wave heights (>2 m) in the last decade is on average less than half of that in the 1985–94 period. We also explored the

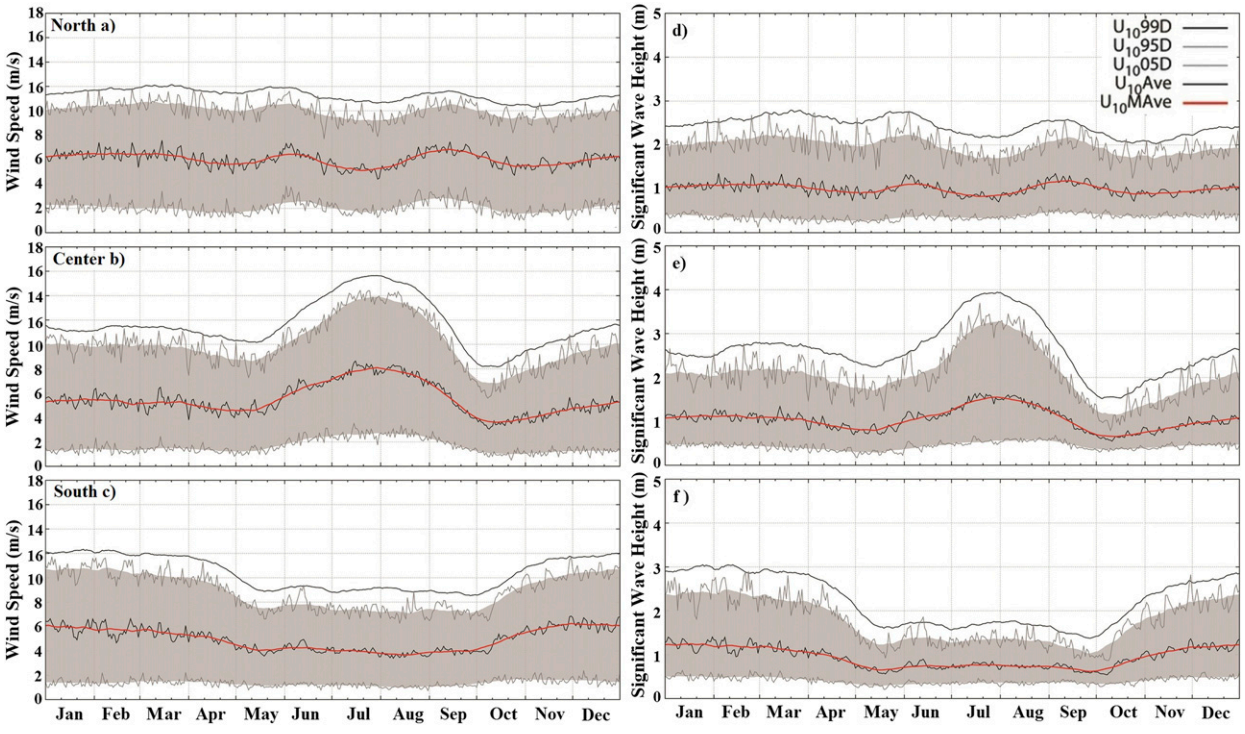


FIG. 4. For each of three zones [(top) N, (middle) C, and (bottom) S] indicated in Fig. 1, (left) wind speed and (right) significant wave height, daily distribution by month of the 99th (black), 95th (gray), and 5th (gray) percentile, and mean (black) and its running average (red).

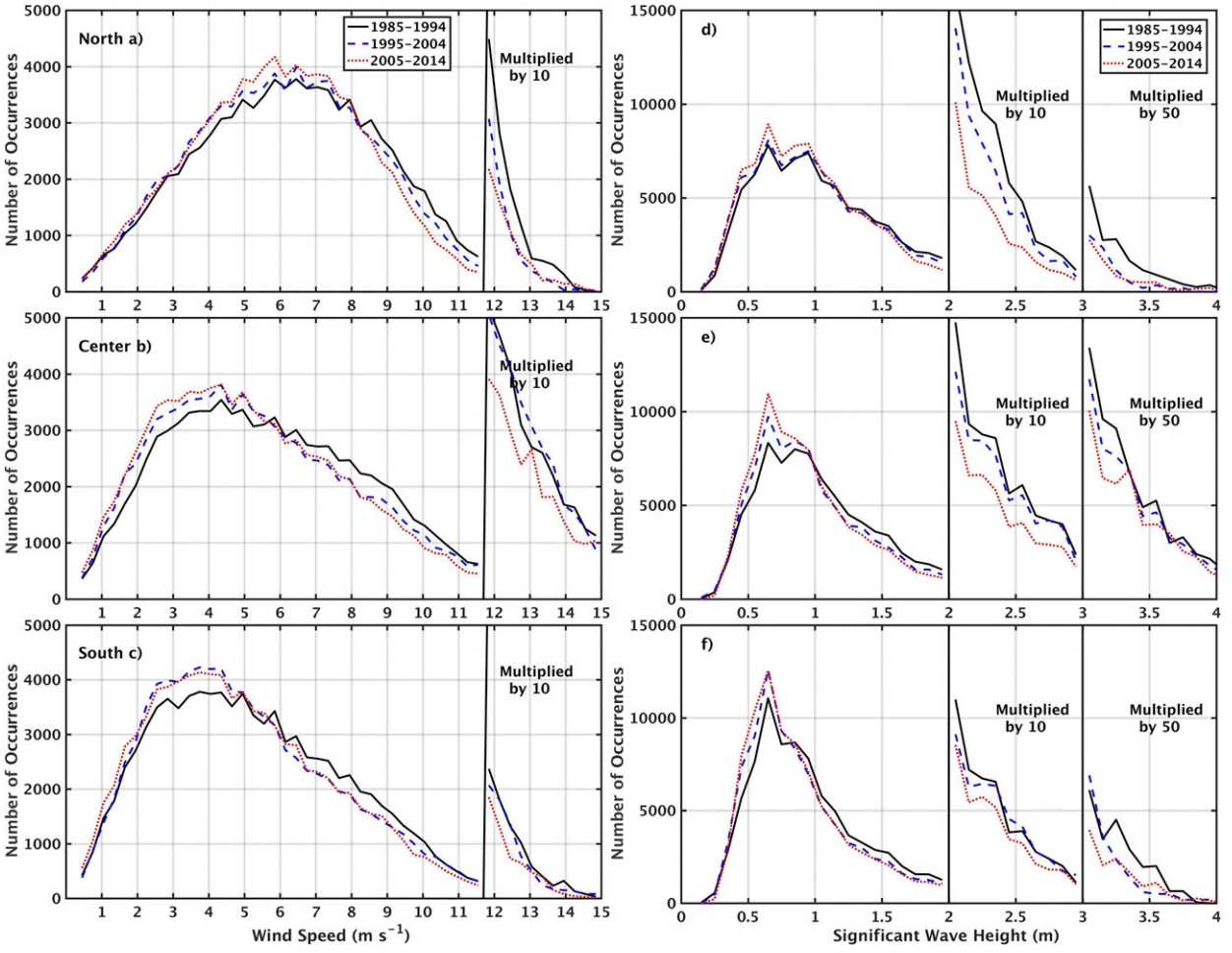


FIG. 5. For (top to bottom) the three zones (N, C, S) indicated in Fig. 1, statistical distributions of (left) wind speed and (right) significant wave height for the first (1985–94, solid black), middle (1995–2004, dashed black), and last decade (2005–14, dotted red) of the 30-yr period are shown. Note the enlarged scale to the right of each distribution.

distribution of this tendency in the basin. Figure 6 displays the trends and best-fit slopes of $U_{10}$ and $H_s$ derived from the whole-time series (more than 260 000 data per grid point) and from the monthly maxima (one datum per month). The whole Red Sea exhibits a negative trend. Although the value alone may have appreciable confidence limits (though >260 000 values provide a solid ground to start from), the overall message is remarkable. The strongest negative trend for mean wind is found in the north and Tokar Gap areas, while the same trends for the monthly maxima are rather spread across the basin. As expected, the wave trends follow accordingly.

One interesting point is the precise identification of where these changes come from. However, the results in Fig. 5 and the trends in Fig. 6 cannot be associated with a specific meteorological pattern. For this, a more powerful and different approach is required. The related tool is described in the next section.

## 6. Spectral partition approach

Wind waves are an integrated product, in space and time, of the driving wind fields. This implies that, to derive the wave conditions at a specified location, the wind fields must be known in space and time. Conversely, the wave conditions at a specific location, specified in frequency and direction (spectrum), provide valuable information about the driving wind fields. A wave spectrum can be split into its composing wave systems, associated with the different physical conditions, where each system is identified by its own energy, peak frequency, and direction. Portilla et al. (2015) exploited this approach to derive the long-term statistics of wave systems acting at given locations. Their paper offers a full description of the method. The partition algorithm works as follows. For each spectrum, from each frequency–direction ($f$–$\theta$) spectral bin,

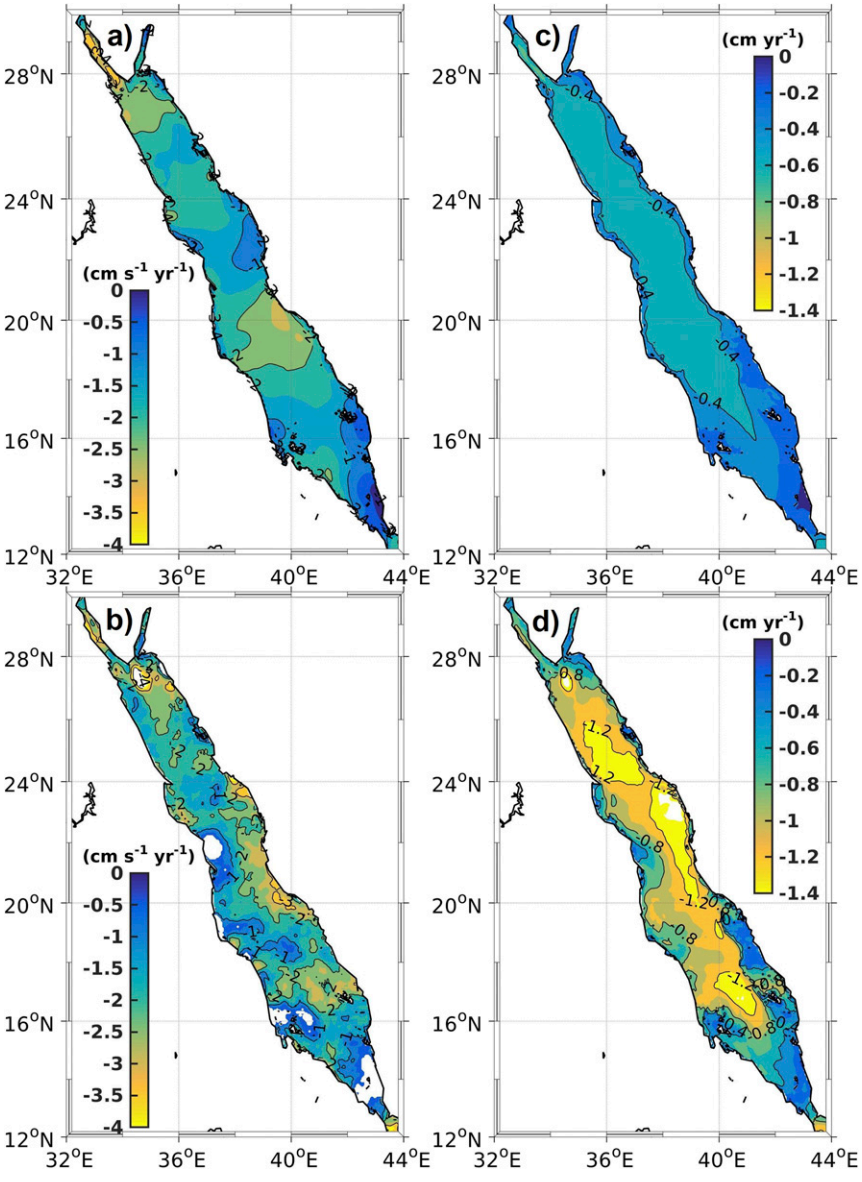


FIG. 6. For (top) wind speed and (bottom) significant wave height, the geographical distributions of the trends are derived by best-fit line to (left) the whole time series and (right) the monthly maxima.

the steepest path of ascending variance density is followed until a local peak is reached. All the points climbing to the same local peak are then grouped to form a partition. This partitioning is not aimed at differentiating between wind seas or swells, but some information can be derived from the physical one embedded in the spectrum. For long series of spectral data, the main advantage of partitioning is a facilitated analysis of the individual wave systems, independently of each other.

We begin our analysis by considering the central points of the three areas of the Red Sea (N, C, and S) and their related spectral information (see section 3). From these long-term spectral data, we derived 30-yr statistics of their partitions and corresponding distributions, shown in Fig. 7 [see Portilla et al. (2015) for details of the procedure]. Still in the two $f$–$\theta$ dimensions, the figure presents the statistical distribution of the positions of the peaks from the different wave systems in all the spectra over the whole 30-yr period. Using the partition technique again, this distribution is then separated into different systems (as in Fig. 7), highlighting and identifying the characteristics (frequency and direction) of the dominant systems. The contours and colors represent

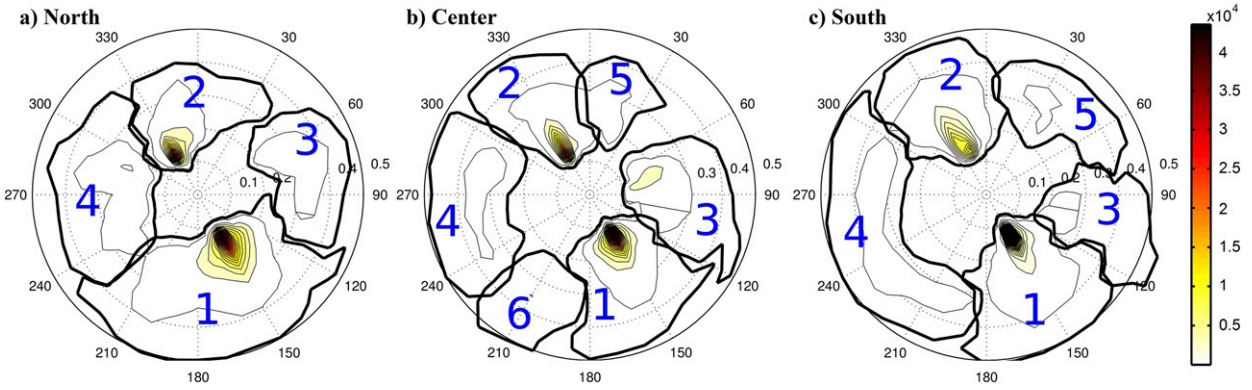


FIG. 7. The long-term distribution of the peak positions that the various wave systems present in each spectrum from the 30-yr time series at a representative central point in the (left to right) north, center, and south zones. Directions are given following oceanographic convention.

how frequently each system appears. Since we are dealing with waves, we follow the oceanographic convention (i.e., we specify the direction of wave propagation).

In Fig. 7, the logical groups have been numbered according to the number of data in each area (i.e., the frequency of appearance for each system). The wave systems in Table 1 are listed in order of their importance. Taking zone C as an example, we recognize the dominant E1 (numbered 1 in the plot) wave system flowing toward 150°, followed by the opposite system E2 (2 in the plot) at 330°. System E3 (3 in the plot) is the result of the Tokar Gap waves at 90°. A few other wave systems are generated by occasional winds in other directions. System E4 (4 in the plot) is in zone N (Fig. 7a). Note that this distribution does not provide any information about the wave height or, more specifically, about the energy that led to the distribution of the systems. However, this information is available from the part of the wave spectra that corresponds to the individual wave systems, which we use for our detailed climatological analysis of these systems.

We repeat the analysis performed in section 4 for the overall significant wave heights on the individual wave systems, as identified from the statistical distribution of the spectral peaks. The first comprehensive result is presented in Fig. 8, where each column refers to a zone (north, center, or south) and each row repeats the yearly distribution (as in Fig. 4), with the first row corresponding to the total energy (ET) of the wave system and the following four rows noting the energy of the E1, E2, E3, and E4 systems, respectively. The total wave energy (ET) is close to the sum of the single systems; the minor differences (<1%) correspond (see Fig. 7) to the energy of the remaining groups in the other directions.

The different panels in Fig. 8 provide an instructive and comprehensive view of the climatological situation. The overall energy characteristics in each of the three areas throughout the year reflect what we already reported in Fig. 4 with the significant wave height. The propagation of southward waves (E1 system) along the Red Sea basin and their corresponding progressive decrease in energy are clearly depicted in the second row of Fig. 8. Conversely, the waves associated with the monsoon (E2 system) and their contributions in the different zones are given in the third row. These waves are virtually absent from May to September; their peaks occur in the winter months. Though the monsoon winds largely affect the southern part of the basin, a small part of the generated waves propagate northward (Fig. 8, two left panels). However, these waves are less effective than system E1 in the northern Red Sea. The isolated effect of the Tokar Gap winds (the fourth row) is macroscopic and present only during the summer months over the central Red Sea. The last row, noticeable only in N, represents the E4 system and corresponds to the mountain valley jets from northern Saudi Arabia during the winter months.

We now explore how the energy of each of the systems, E1, E2, E3, and E4, varied over the 30-yr time span in each area, N, C, and S. Since the seasonality of the signal was evident given the results shown in Fig. 8, a monthly trend analysis was applied. Rather than using a single best-fit line fit, the trends were evaluated following first the Mann–Kendall approach (Mann 1945; Kendall 1975) and then quantified following Sen (1968). Pomaro et al. (2017) provide a full description of the procedure followed for this analysis. The results are shown in Fig. 9 following the same order as Fig. 8: left to right corresponds to north, center, and south; top to

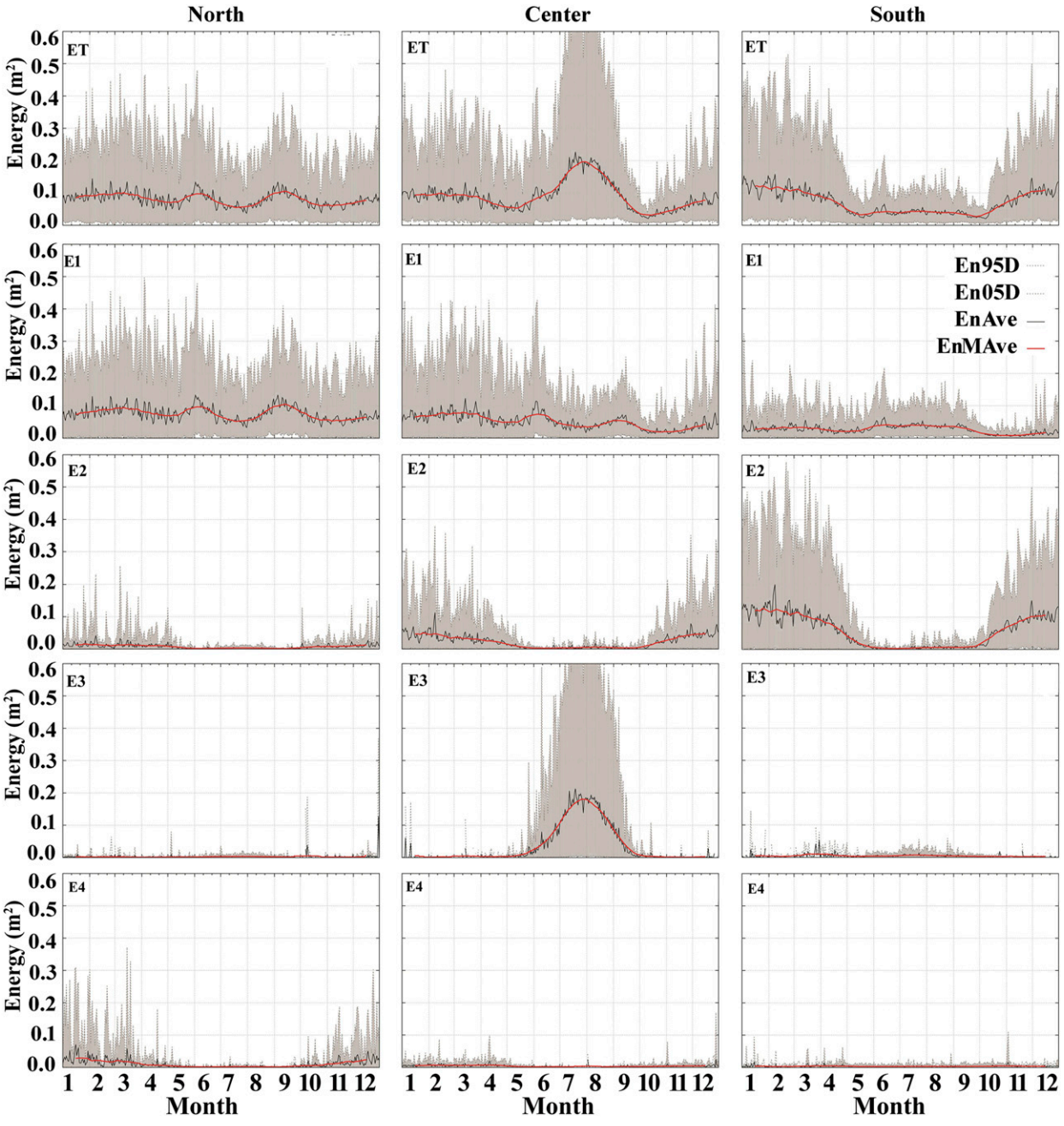


FIG. 8. (left to right) The north, central, and south zones in Fig. 1. (top to bottom) The total wave energy throughout the year and the energy of the E1, E2, E3, and E4 systems. The 95th percentile (dotted gray), mean (solid black), running-averaged mean (solid red), and 5th percentile (dotted gray) are shown. Each row shows how the energy of each system varies throughout the basin.

bottom corresponds to trends in energy for total energy (ET), E1, E2, E3, and E4. Note that a circle represents the signals with significance over the 90% level. In each panel, the 99th-, 95th-, 75th-, and 50th-percentile trends are shown.

The results in Fig. 9 show a diffused negative trend. However, splitting the ET signal (first row) among the different components allows us to identify which systems and which zones contribute more to this trend. In general, system E1 has the largest contribution in all three zones. Considering the different E1 energy in N and S shown in Fig. 8, the relative change is more macroscopic in S. This suggests that the pulses of cold air from the Mediterranean Sea are not only progressively losing strength, but that this also corresponds to a decreased ability to propagate energy toward the south.

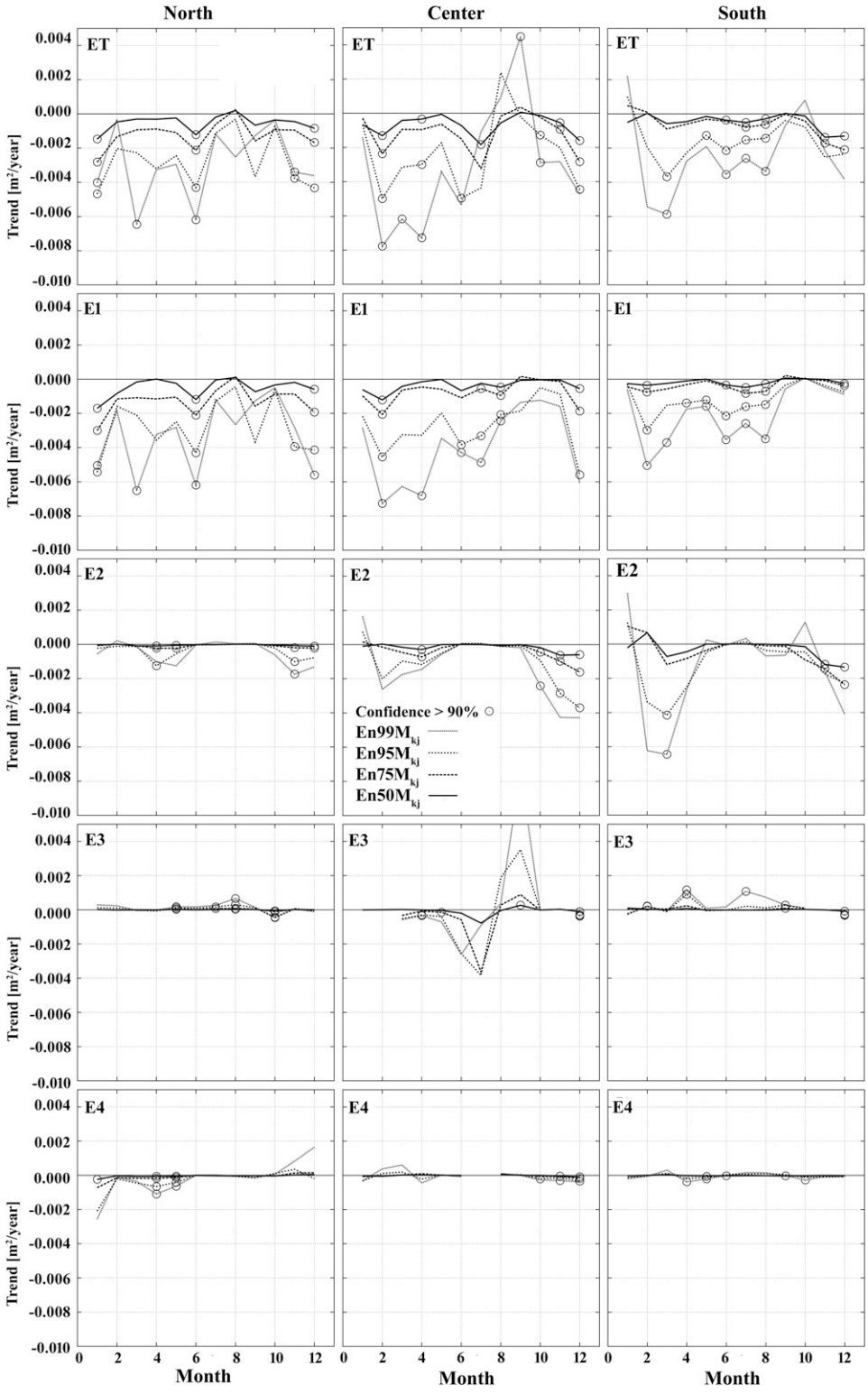


FIG. 9. The energy value trends for each month of the year presented with the same logical distribution as in Fig. 8. The trends of the 99th (close dotted black), 95th (dotted black), 75th (dashed black), and 50th (solid black) percentiles are shown. A circle indicates that the result is statistically significant at better than 90%.

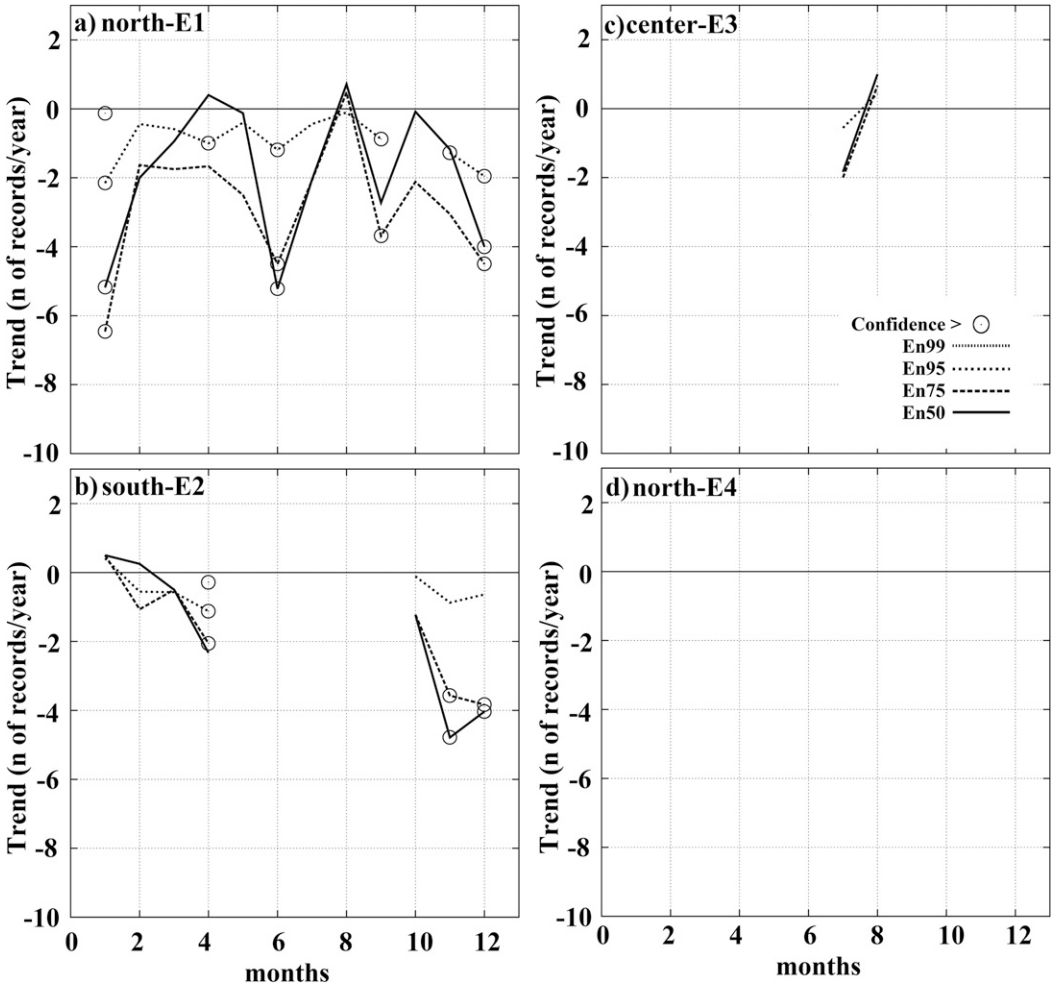


FIG. 10. Trend in the number of data for each month of the year. The results are shown only for the months where a sufficient number of data is present: (a) E1 and (d) E4 in the north, (b) E2 in the south, and (c) E3 in center. The results of the 99th, 95th, 75th, and 50th percentiles are shown (same line legend as in Fig. 9). A circle indicates that the result is statistically significant at better than 90%.

There is also less energy in the monsoon-connected wind and waves (E2) in S, particularly during the early months of the year, but this weakness is only statistically significant in March. This decrease is reflected in C and N by progressively lower signals, consistent with the energy shown in Fig. 8. There are no significant trends found in the Tokar Gap waves (E3). Finally, there is a very mild but significant negative signal for the E4 system in N, which is proportional to the local energy.

In plotting the energy and the related trends in Figs. 8 and 9, it is not clear whether the energy loss in time is due to the reduced strength of individual storms or to their decreasing number. We explored this by analyzing the frequency of the hourly data (i.e., how the number of occurrences of these records per year has varied in time; results shown in Fig. 10). We show only the relevant results for E1 in N, E2 in S, E3 in C, and E4 in N. There is a substantial reduction in the number of hourly events for E1, up to six per year in January for the 50th and 75th percentiles, with significant values also in June and December. Also, the number of monsoon events seems to decrease in the last months of each year, but this is uniformly significant. We have not found any trends in the number of the Tokar Gap events or in those connected to the E4 system.

## 7. Summary and discussion

The main findings of our work can be summarized as follows.

1) Four main wind and wave systems dominate the climate of the Red Sea (see Fig. 1):
   (i) E1 system from north to south, driven by pulses entering from the Mediterranean Sea;

(ii) E2 system from south to north, associated with the northeast monsoon channeled through the Bab el Mandeb Strait;
(iii) E3 winds blowing from Africa through the Tokar Gap, generating waves toward the Arabian Peninsula; and
(iv) E4 system, generated by jets from valleys in the northern part of the Arabian Peninsula.

2) The different features support splitting the Red Sea into three zones for the analysis, namely, north (N), center (C), and south (S).
3) N is dominated by the E1 system, with minor contributions from E4 and sometimes E2 waves that reach the northern end of the Red Sea.
4) The dominant feature in C during summer is the E3 system. Otherwise, it is mostly dominated by E1 waves from the north and partly by E2 waves from the south in winter.
5) The monsoon-connected E2 system is the main one in S, with E1 waves frequently reaching this area.
6) On average, the highest waves are in N, but the peak values are reached in C with the E3 system.
7) Though at a variable level, the E1 system is present throughout the year; the other three systems are markedly seasonal, with E2 and E4 in the winter season and E3 in the summer months.
8) There is a marked tendency toward decreasing wave heights in the Red Sea.
9) The partition technique allows a better definition of the characteristics and trends of each system.
10) The most marked decrease, both in total energy and number of events, is found in the E1 system.
11) A milder decrease, but limited to the first months of the year, appears in E2. However, there is an indication of decreased frequency in the last months of the year.
12) There are no marked trends for the E3 and E4 systems.

Having framed the situation, some of these aspects deserve more general comments.

With the exception of an isolated positive peak in the 99th percentile during September, the marked decrease in both total energy and frequency of the E1 system is quite evident. Since it depends on input from the Mediterranean Sea, we naturally connect this decrease to the corresponding decrease in wind activity in this basin [see, among others, Conte and Lionello (2013)]. The decrease of E2, the monsoon-related southern winds, is more limited, in both intensity and frequency of events. The only significant signal is observed in March; however, that is not a period when we expect intense events.

The strong contrast between the desert-land and sea surface temperatures along the Red Sea coastline results in ageostrophic nighttime land breezes and daytime sea breezes that occur almost daily and in all months (Jiang et al. 2009; Pedgley 1974). Though the dominant wave systems are E1 and E2, the cross-axis winds generate multiple wave systems at all locations in the Red Sea. In summer, the most prominent cross-basin wind blows from the Tokar Gap, which frequently channels strong winds across the center of the Red Sea. These events are largely associated with the Indian summer monsoon, but are further enhanced by the local orography and the large variations between the day and night temperatures on the African high plains. Our analysis did not reveal any appreciable trend in the waves related to the Tokar Gap wind. The overall connection with the summer monsoon is a much broader subject that we did not address in this study.

A comparison between E2 and E4 in the northern sector, where the Arabian Peninsula valleys are located, suggests a possible relationship between the two systems. The E4 winds generally blow from the northeast, a large-scale flow that leads to the E2 winds. Without a direct causality between the two systems, we only hypothesize a possible relationship that is beyond the scope of this paper. Rather, this takes us to a more general point. The wave conditions at a given time and location provide valuable information about the generated wind fields (i.e., previous meteorological situations). If we expand this in time, the wave climate trends provide quite a bit of information about the meteorological ones. This is more striking in the applied partition technique where we can detect changes at one or more positions according to the wave system we observe, the direction it comes from, and potentially other information. This technique is most effective in the ocean because it is possible to analyze the variation of peak frequency of a system in time (days) in order to obtain an estimate of the wave generation zone (even 10 000 km away or more; e.g., Snodgrass et al. 1966). Thus, the trend in time (years) of a wave system may tell us something about faraway winds (see, e.g., Portilla et al. 2015). This is not straightforward, if at all possible, for the waves in the Red Sea. Rather, the elongated shape of the sea and its mountain border highly simplify the diagnosis. In this relatively simple environment, we are able to derive information about the larger surrounding areas.

The presence of a trend derived from a reanalysis of the meteorological data starting from the ERA-Interim deserves a discussion. It is well known that changes in the number and quality of the assimilated measured data may have, and had in ERA-Interim, a significant influence, especially on the derived trends.

The paper by Aarnes et al. (2015) is enlightening in this respect. Especially in a reanalysis inevitably generated at a limited resolution, there is a general tendency to underestimate high values, a trend that is eventually corrected by the assimilation of measured data. In the long term, the progressively increased quality and quantity of these data may lead to an apparent positive trend in the reanalysis. However, the trends we found are negative, therefore arguably independent and more reliable. If any doubt remains, it is that the real negative trends may be even larger than what we report.

Although we do not venture into large-scale climatic analysis in this paper, we find one strong connection possibly supported our results. Conte and Lionello (2013), among others, report, as repetitively seen in other studies, an attenuation of the wind and wave climate in the Mediterranean Sea. It can be said that the climate is shifting northward. If this is the case, then the latitudinal gradients would decrease in the Mediterranean Sea and, in doing so, would also decrease the differences with respect to the Red Sea (via the Suez and possibly Aqaba gulfs). Indeed, this can be interpreted as the reason for the decreased intensity and frequency of the Mediterranean pulses.

The reasons for the described variations in time involve a broader scale of analysis with respect to the identification we pursued in this paper with the 30-yr hindcast. However, with a reversed perspective, it is interesting to analyze the oceanographic implications of a varying wave climate in the Red Sea. Wu et al. (2015) have recently framed well the importance of wind waves in defining the vertical structure of the ocean. Together with surface breaking, Stokes drift, and Langmuir circulation, they pointed out to the importance of wave orbital motion in stirring the upper layers of the ocean and deepening the thermocline (see also Huang and Qiao 2010). In this respect, the decrease of wave height, especially of the E1 system, is not without consequences. Being locally wind generated, a decrease of the significant wave height also implies a decrease of the corresponding wavelength (see, e.g., Holthuijsen 2007). Given the wave-induced motion and exponential attenuation with depth, a decrease of wind, consequently waves (hence their length), may have immediate consequences on the depth of the mixed layers, which reflects the extent of vertical mixing.

The reported decreasing of the wind speed can potentially affect the formation of the Red Sea outflow water, which is formed in the north during winter under the conditions of intensive heat loss (Yao et al. 2014). The heat loss would be reduced by the decreased wind speed, because of the linear dependence of the turbulent heat flux, and the latent and sensible heat fluxes on the wind speed. The reduced mixed layer depth associated with the decreasing waves would change the properties of the formed water. Therefore, if the present trend continues, the outflow of the Red Sea water to the Indian Ocean is likely to change, and hence the signature of the Red Sea water along the eastern African coastline (Beal et al. 2000). Indeed, it is very interesting how limited changes in the atmospheric distribution over a semi-enclosed basin could lead to significant changes in the adjacent large oceans.

Can we say anything about the future? We only have information for 30 yr; we need more data before and after this period. A comparison between the values in Fig. 8 and Fig. 9 suggests loss of wave heights on the order of 1% $yr^{-1}$ (e.g., for the E1 system in N). This decrease is quite significant, and not unlike other estimates for the Mediterranean Sea [see the cited paper by Conte and Lionello (2013)]. More information could be derived from climatic projections, but their present coarse resolutions and variable background hypotheses persuade us to be satisfied for the time being with the more limited, but solid, information we have derived.

*Acknowledgments.* The research reported in this publication was supported by funding from King Abdullah University of Science and Technology (KAUST). It also made use of the Supercomputing Laboratory and computer clusters at KAUST. Sabique Langodan was supported by the General Commission of Survey (GCS), under Project RGC/3/1612-01-01 made by Office of Sponsored research (ORS)/KAUST, Kingdom of Saudi Arabia. Luigi Cavaleri was partly supported by KAUST during his visits for research collaboration and, together with Angela Pomaro, by E.U. Contract 730030 (H2020-EO-2016, ''CEASELESS''). Three anonymous reviewers and the editor, Oleg A. Saenko, provided valuable suggestions leading to an improvement of the paper.

## APPENDIX

### Validation of Model Simulations

The model outputs were validated using observations from buoy, scatterometer, and altimeter data. The buoy (WMO 23020, located at 22°10′N, 38°30′E and depth of 693 m) was deployed from October 2008 until May 2010. All of the available altimeter (*Jason-1*, *Jason-2*, *ERS-1*, *ERS-2*, *GFO*, *Envisat*, *Cryosat-2*, *Altika*) data were used ($\sim 4 \times 10^5$ collocated points) as

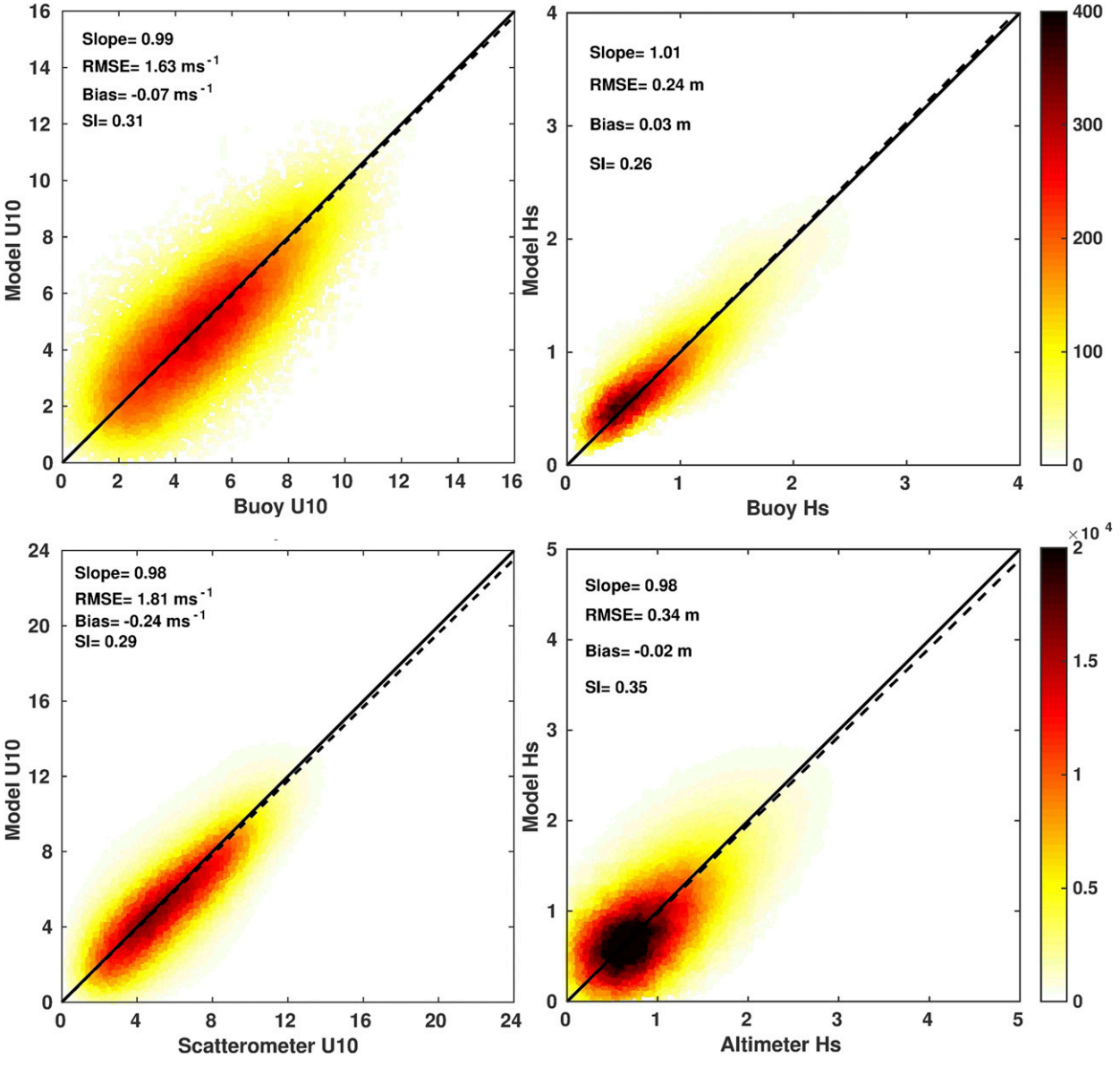


FIG. A1. Scatter diagrams and best-fit slopes for (left) simulated wind and (right) wave heights against buoy and satellite observations. The color bar indicates the number of collocated points. The statistics—slope, rmse, bias, and scatter index—are labeled on figure.

derived from the GlobWave database (http://www.globwave.org) for validation. The scatterometer data that are not assimilated were used for validation. Figure A1 presents the scatterplots of the model fields from the buoy, scatterometer, and altimeter data. The various panels show the corresponding scatter diagrams, with the colors representing the number of collocated points in each pixel. A best-fit line is overlaid on the scatterplot. The statistics show that the model fields are in good agreement with the measurements. Moreover, the statistical parameters computed from the altimeter and scatterometer data are in the same range as those from the buoy observations.

## REFERENCES

Aarnes, O. J., S. Abdalla, J.-R. Bidlot, and O. Breivik, 2015: Marine wind and wave height trends at different ERA-Interim forecast ranges. *J. Climate*, **28**, 819–837, https://doi.org/10.1175/JCLI-D-14-00470.1.

Aboobacker, V. M., P. R. Shanas, M. A. Alsaafani, and M. A. Albarakati, 2016: Wave energy resource assessment for Red Sea. *Renew. Energy*, **114**, 46–58, https://doi.org/10.1016/j.renene.2016.09.073.

Appendini, C. M., A. Torres-Freyermuth, P. Salles, J. López-González, and E. Mendoza, 2014: Wave climate and trends for the Gulf of Mexico: A 30-yr wave hindcast. *J. Climate*, **27**, 1619–1632, https://doi.org/10.1175/JCLI-D-13-00206.1.

Ardhuin, F., and Coauthors, 2010: Semiempirical dissipation source functions for ocean waves. Part I: Definition, calibration, and

validation. *J. Phys. Oceanogr.*, **40**, 1917–1941, https://doi.org/10.1175/2010JPO4324.1.

Beal, L. M., A. Ffield, and A. Gordon, 2000: Spreading of Red Sea overflow waters in the Indian Ocean. *J. Geophys. Res.*, **105**, 8549–8564, https://doi.org/10.1029/1999JC900306.

Caires, S., V. R. Swail, and X. L. Wang, 2006: Projection and analysis of extreme wave climate. *J. Climate*, **19**, 5581–5605, https://doi.org/10.1175/JCLI3918.1.

Charles, E., D. Idier, J. Thiébot, G. Le Cozannet, R. Pedreros, F. Ardhuin, and S. Planton, 2012: Present wave climate in the Bay of Biscay: Spatiotemporal variability and trends from 1958 to 2001. *J. Climate*, **25**, 2020–2039, https://doi.org/10.1175/JCLI-D-11-00086.1.

Conte, D., and P. Lionello, 2013: Characteristics of large positive and negative surges in the Mediterranean Sea and their attenuation in future climate scenarios. *Global Planet. Change*, **111**, 159–173, https://doi.org/10.1016/j.gloplacha.2013.09.006.

Dee, D. P., and Coauthors, 2011: The ERA-Interim reanalysis: Configuration and performance of the data assimilation system. *Quart. J. Roy. Meteor. Soc.*, **137**, 553–597, https://doi.org/10.1002/qj.828.

Fery, N., G. Bruss, A. Al-Subhi, and R. Mayerle, 2012: Numerical study of wind-generated waves in the Red Sea. *Proc. 4th Int. Conf. on the Application of Physical Modeling to Port and Coastal Protection*, Coastlab12, Ghent, Belgium, 446–455.

Gulev, S. K., V. Grigorieva, A. Sterl, and D. Woolf, 2003: Assessment of the reliability of wave observations from voluntary observing ships: Insights from the validation of a global wind wave climatology based on voluntary observing ship data. *J. Geophys. Res.*, **108**, 3236, https://doi.org/10.1029/2002JC001437.

Hasselmann, S., K. Hasselmann, J. H. Allender, and T. P. Barnett, 1985: Computations and parameterizations of the nonlinear energy transfer in a gravity-wave spectrum. Part II: Parameterizations of the nonlinear transfer for application in wave models. *J. Phys. Oceanogr.*, **15**, 1378–1391, https://doi.org/10.1175/1520-0485(1985)015<1378:CAPOTN>2.0.CO;2.

Holthuijsen, L. H., 2007: *Waves in Oceanic and Coastal Waters*. Cambridge University Press, 387 pp.

Huang, C. H., and F. Qiao, 2010: Wave-turbulence interaction and its induced mixing in the upper ocean. *J. Geophys. Res.*, **115**, C04026, https://doi.org/10.1029/2009JC005853.

Janssen, P. A. E. M., 1991: Quasi-linear theory of wind-wave generation applied to wave forecasting. *J. Phys. Oceanogr.*, **21**, 1631–1642, https://doi.org/10.1175/1520-0485(1991)021<1631:QLTOWW>2.0.CO;2.

Jiang, H., J. T. Farrar, R. C. Beardsley, R. Chen, and C. Chen, 2009: Zonal surface wind jets across the Red Sea due to mountain gap forcing along both sides of the Red Sea. *Geophys. Res. Lett.*, **36**, L19605, https://doi.org/10.1029/2009GL040008.

Kendall, M. G., 1975: *Rank Correlation Methods*. 4th ed. Charles Griffin, 160 pp.

Kushnir, Y., V. J. Cardone, J. G. Greenwood, and M. A. Cane, 1997: The recent increase in North Atlantic wave heights. *J. Climate*, **10**, 2107–2113, https://doi.org/10.1175/1520-0442(1997)010<2107:TRIINA>2.0.CO;2.

Langodan, S., L. Cavaleri, Y. Viswanadhapalli, and I. Hoteit, 2014: The Red Sea: A natural laboratory for wind and wave modeling. *J. Phys. Oceanogr.*, **44**, 3139–3159, https://doi.org/10.1175/JPO-D-13-0242.1.

——, ——, ——, and ——, 2015: Wind wave source functions in opposing seas. *J. Geophys. Res. Oceans*, **120**, 6751–6768, https://doi.org/10.1002/2015JC010816.

——, Y. Viswanadhapalli, H. P. Dasari, O. Knio, and I. Hoteit, 2016: A high resolution assessment of wind and wave energy potentials in the Red Sea. *Appl. Energy*, **181**, 244–255, https://doi.org/10.1016/j.apenergy.2016.08.076.

Liu, Q., A. V. Babanin, S. Zieger, I. R. Young, and C. Guan, 2016: Wind and wave climate in the Arctic Ocean as observed by altimeters. *J. Climate*, **29**, 7957–7975, https://doi.org/10.1175/JCLI-D-16-0219.1.

Mann, H. B., 1945: Nonparametric tests against trend. *Econometrica*, **13**, 245–259, https://doi.org/10.2307/1907187.

Metwally, A., and A. G. Abul-Azm, 2007: The Red Sea wind-wave ATLAS. *Proc. 17th Int. Offshore and Polar Engineering Conf.*, Lisbon, Portugal, International Society of Offshore and Polar Engineers, 1850–1854.

Pedgley, D. E., 1974: An outline of the weather and climate of the Red Sea. *L'Oceanographie Physique de la Mer Rouge: Symp. de l'Association International des Sciences Physiques de l'Océan*, Paris, France, UNESCO, 9–27.

Pomaro, A., L. Cavaleri, and P. Lionello, 2017: Climatology and trends of the Adriatic Sea wind waves: Analysis of a 37-year long instrumental data set. *Int. J. Climatol.*, **37**, 4237–4250, https://doi.org/10.1002/joc.5066.

Portilla, J., L. Cavaleri, and G. P. van Vledder, 2015: Wave spectra partitioning and long term statistical distribution. *Ocean Modell.*, **96**, 148–160, https://doi.org/10.1016/j.ocemod.2015.06.008.

Ralston, D. K., H. Jiang, and T. F. Ferrar, 2013: Waves in Red Sea: Response to monsoonal and mountain gap winds. *Cont. Shelf Res.*, **65**, 1–13, https://doi.org/10.1016/j.csr.2013.05.017.

Semedo, A., S. K. Rutgersson, and A. Sterl, 2011: A global view on the wind sea and swell climate and variability from ERA-40. *J. Climate*, **24**, 1461–1479, https://doi.org/10.1175/2010JCLI3718.1.

——, R. Vettor, Ø. Breivik, A. Sterl, M. Reistad, C. G. Soares, and D. Lima, 2015: The wind sea and swell waves climate in the Nordic seas. *Ocean Dyn.*, **65**, 223–240, https://doi.org/10.1007/s10236-014-0788-4/

Sen, P. K., 1968: Estimate of the regression coefficients based on Kendall's tau. *J. Amer. Stat. Assoc.*, **63**, 1379–1389, https://doi.org/10.2307/2285891.

Skamarock, W. C., and Coauthors, 2008: A description of the Advanced Research WRF version 3. NCAR Tech. Note NCAR/TN-475+STR, 113 pp., https://doi.org/10.5065/D68S4MVH.

Snodgrass, F. E., G. W. Groves, K. F. Hasselmann, G. R. Miller, W. H. Munk, and W. M. Powers, 1966: Propagation of swell across the Pacific. *Philos. Trans. Roy. Soc. London*, **259A**, 431–497, https://doi.org/10.1098/rsta.1966.0022.

Tolman, H. L., 2014: User manual and system documentation of WAVEWATCH-III version 4.18. NOAA/NWS/NCEP/OMB Tech. Note 316, 311 pp.

Tuomi, L., K. Kahma, and H. Pettersson, 2011: Wave hindcast statistics in the seasonally ice-covered Baltic Sea. *Boreal Environ. Res.*, **16**, 451–472.

Vinoth, J., and I. R. Young, 2011: Global estimates of extreme wind speed and wave height. *J. Climate*, **24**, 1647–1665, https://doi.org/10.1175/2010JCLI3680.1.

Wang, X. L., and V. R. Swail, 2001: Changes in extreme wave heights in Northern Hemisphere oceans and related atmospheric circulation regimes. *J. Climate*, **14**, 2204–2221, https://doi.org/10.1175/1520-0442(2001)014<2204:COEWHI>2.0.CO;2.

Wu, L., A. Rutgersson, and E. Sahlée, 2015: Upper-ocean mixing due to surface gravity waves. *J. Geophys. Res. Oceans*, **120**, 8210–8228, https://doi.org/10.1002/2015JC011329.

Yao, F., I. Hoteit, L. J. Pratt, A. S. Bower, A. Köhl, G. Gopalakrishnan, and D. Rivas, 2014: Seasonal overturning circulation in the Red Sea: 2. Winter circulation. *J. Geophys. Res. Oceans*, **119**, 2263–2289, https://doi.org/10.1002/2013JC009331.